(Received 16 May 2026, Accepted 15 July 2026, Scheduled 4 September 2026)

Impact of Magnetic Saturation on Back-EMF in PMSMs Using a Hybrid Analytical Approach

Samir Mezghiche[1,*], Brahim Ladghem-Chikouche[1], Lazhar Roubache[2], and Zakarya Djelloul-Khedda[3]

[1]Department of Electrical Engineering, Faculty of Technology, University of M'sila, M'sila 28000, Algeria
[2]Department of Electrical Engineering, High School of Applied Sciences of Algiers ESSAA Bab El-Oued, Algiers, Algeria
[3]LESI Laboratory, Djilali Bounaama University, Khemis Miliana, Algeria

ABSTRACT: Fast, accurate modeling of permanent magnet synchronous machines (PMSMs) is essential for efficient design optimization, particularly in high-power wind turbine applications where severe magnetic saturation frequently occurs. While pure analytical models offer rapid computation, they often fail to accurately account for nonlinear saturation, which significantly affects the machine's performance, particularly the back-electromotive force (back-EMF). This study proposes a computationally efficient 2D hybrid analytical framework to investigate the impact of magnetic saturation on the back-EMF in PMSMs. The proposed approach couples an exact analytical subdomain (SD) technique, which is used to resolve the magnetic field in linear regions, with a nonlinear magnetic equivalent circuit (MEC) model for the active ferromagnetic parts. By iteratively updating the relative permeability in the MEC, the method accurately captured local saturation effects and reflected them in the global air-gap flux density. The developed hybrid analytical model (HAM) was used to analyze the total harmonic distortion (THD) and peak values of the back-EMF under saturated conditions. To validate the proposed method, results were compared with those obtained from a 2D finite element analysis (FEA). The comparison shows that the hybrid approach achieves an excellent compromise, delivering a high accuracy comparable to that of the FEA while drastically reducing computational time, making it highly suitable for iterative design and optimization process.

1. INTRODUCTION

Permanent magnet synchronous machines (PMSMs) have become a preferred topology for high-power wind energy conversion systems owing to their high torque density, operational reliability, and high efficiency [1–3]. The rigorous design and optimization of these large-scale generators require precise modeling tools to maximize their performance while minimizing active material volumes [4–6]. A fundamental aspect of PMSM design is accurately evaluating the magnetic flux distribution. To achieve high power densities, the ferromagnetic components of the machine, specifically the stator teeth and yoke, frequently operate deep within the nonlinear magnetic saturation region [7, 8]. This localized saturation heavily distorts the air-gap flux density, directly altering induced back-electromotive force (back-EMF). Accurately predicting the saturated back-EMF waveform and its harmonic content is essential because it governs the electrical output quality and overall performance of the generator [9–11].

Review of Existing Approaches

The system of partial differential equations (PDEs) derived from Maxwell's equations for electrical machines is generally solved using three main categories of methods [12–14], each offering different compromises among accuracy, computational speed, and handling magnetic nonlinearity.

- **Numerical Methods:** The widely used approach relies on numerical discretization, such as finite element analysis (FEA) [15], and the finite difference method (FDM) [16]. While FEA serves as the gold standard for handling complex geometries and severe magnetic saturation, its high computational cost, which often requires significant execution time per iteration, makes it prohibitive for early-stage parametric optimization of large-scale generators, where thousands of design evaluations are necessary [17–19].
- **Analytical Methods:** Alternatively, analytical Maxwell-Fourier methods (including multilayer models, eigenvalue models, and exact analytical subdomain (SD) techniques) [20–23] and Schwarz-Christoffel mapping [24] offer rapid, continuous field solution. In these approaches, harmonic series are formulated by applying the separation of variables to solve Laplace's and Poisson's equations with strict boundary conditions. Extended SD techniques have attempted to include the iron core by assuming a finite and constant relative permeability [25]. However, this assumption fails under saturated conditions: a constant permeability cannot capture localized, nonlinear reluctance variations caused by severe flux concentration in the stator teeth, leading to significant inaccuracies in predicting back-EMF waveform [18, 26].
- **Hybrid Methods:** To combine the benefits of the model's analytical speed and numerical handling of nonlinearity, recent research has shifted towards hybrid methods. Var-

* Corresponding author: Samir Mezghiche (samir.mezghiche@univ-msila.dz).

TABLE 1. Quantitative comparison of electromagnetic modeling methods.

Methodology	Saturation Handling	Accuracy	Computational Cost	Convergence Characteristics	Suitability for Iterative Design
Numerical (FEA/FDM)	Excellent (Inherent)	Very High	Very High	Guaranteed (mesh-dependent, slow)	Low
Analytical (SD)	Poor (Linear assumption)	Low (if saturated)	Very Low	Direct (non-iterative, closed-form)	High (Linear only)
Hybrid	High (Iterative updating)	High	Low	Fast (17 iterations for the studied case)	Very High

ious coupling strategies have been proposed in the literature; however, a critical analysis reveals specific limitations for large-scale machine design:

- Coupling FEA with magnetic equivalent circuit (MEC) [27]: While highly accurate, the reliance on FEA for sub-regions still imposes a considerable computational burden, negating speed advantages required for rapid iterative design.
- Combining conformal mapping with MEC [28]: This approach provides rapid evaluations but becomes mathematically restrictive and struggles to maintain accuracy for complex, highly saturated slotted geometries.
- Interfacing Maxwell-Fourier methods with FEA [29]: This strategy often suffers from complex boundary matching and mesh-transition issues between analytical and numerical domains, slowing down convergence.
- Coupling FDM with FEA or analytical models [30]: Similar to FEA coupling, a discrete numerical grid introduces significant computational overhead.
- Coupling analytical SD techniques with MEC: A direct bidirectional coupling between an exact SD formulation and a MEC has also been proposed, allowing flux continuity to be enforced in both radial and tangential directions at the interface [31]. However, this coupling has been validated only for fixed relative permeability values. Consequently, to account for nonlinearities, several recent works have combined analytical formulations with a MEC to evaluate saturation [32–34]. Nevertheless, these methods typically model the saturation through simplified approaches, such as an equivalent surface current or a single permeance per tooth. As a result, these hybrid techniques remain either computationally intensive or mathematically rigid, rendering them inadequate for PMSMs' rapid, large-scale iterative design. To systematically compare these trade-offs, Table 1 summarizes the performance metrics of the existing modeling categories [35, 36].

To overcome these limitations, this work extends this class of methods through a finely discretized nodal MEC, whose local reluctances are updated iteratively from the measured B-H curve, bidirectionally coupled to the SD formulation using boundary flux injection. The approach is applied specifically to quantify the resulting distortion of the back-EMF harmonic spectrum in large-scale wind turbine PMSMs.

2. ANALYTICAL SD FORMULATION

The analytical framework requires partitioning the machine's cross-section into three SDs as illustrated in Figure 1: stator slots, air gap, and permanent magnets (PMs).

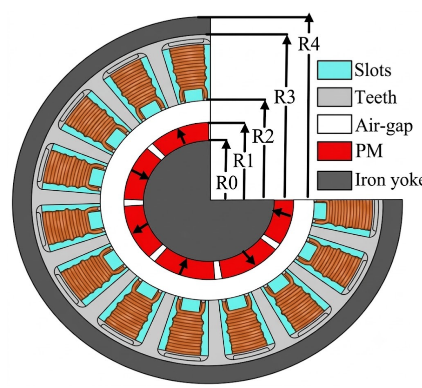

FIGURE 1. Studied PMSM geometry.

To evaluate the magnetic field distribution within these regions, the problem was formulated using the magnetic vector potential. Under a 2D approximation, only the axial component A_z is considered [20, 21]. By applying Maxwell's equations within a polar coordinate system (r, θ), the behavior of the magnetic field is governed by a generalized Poisson's equation given in (1a), where J_z represents the imposed axial current density; μ_0 denotes the permeability of free space; and M is the remanent magnetization vector, which is strictly zero outside the magnet SD.

$$\nabla^2 A_z = -\left[\mu_0 J_z + \mu_0 (\nabla \times M)_z\right] \tag{1a}$$

In region I (PM region)

$$\nabla^2 A_z = -\mu_0 (\nabla \times M)_z \tag{1b}$$

In region II (Air region)

$$\nabla^2 A_z = 0 \tag{1c}$$

In region III (Slots region)

$$\nabla^2 A_z = -\mu_0 J_z \tag{1d}$$

The field vectors $\vec{B}$ and $\vec{H}$ are coupled by:

In region I

$$\vec{B} = \mu_0 \mu_m \vec{H} + \mu_0 \vec{M} \tag{2a}$$

In regions II and III

$$\vec{B} = \mu_0 \vec{H} \tag{2b}$$

where μ_m is the relative permeability of the PMs, and the remanent magnetization vector M is expressed in polar coordinates as:

$$M(\theta) = M_r(\theta)\, e_r + M_\theta(\theta)\, e_\theta \tag{2c}$$

where M_r and M_θ are radial and tangential components of the magnetization vector, respectively, such that e_r and e_θ are unit vectors of the polar basis in radial and tangential directions, respectively. A Fourier expansion for (2c) yields:

$$M_r(\theta) = \sum_{n=1,3,5,..}^{nh} M_{nr}^{s} \sin(np\theta) + M_{nr}^{c} \cos(np\theta) \tag{2d}$$

$$M_\theta(\theta) = \sum_{n=1,3,5,..}^{nh} M_{n\theta}^{s} \sin(np\theta) + M_{n\theta}^{c} \cos(np\theta) \tag{2e}$$

where M_{nr}^s, M_{nr}^c, $M_{n\theta}^s$, and $M_{n\theta}^c$ of (2d) and (2e) are the Fourier coefficients evaluated over one electrical period; n is the harmonic order; p is the number of pole pairs; and nh is the total number of retained harmonics.

The magnetic flux density is related to the magnetic vector potential as follows:

$$\vec{B} = \nabla \times \vec{A} \tag{2f}$$

Using (2f), radial and tangential components of the magnetic flux density are deduced from A_z by:

$$B_r = \frac{1}{r}\frac{\partial A_z}{\partial \theta} \tag{2g}$$

$$B_\theta = -\frac{\partial A_z}{\partial r} \tag{2h}$$

In the PM region (SD I), assuming a vanishing tangential flux density at the lower boundary [21], Equation (1b) is solved using the variable separation method, and the general solution is constructed by combining its homogeneous and particular components. For an arbitrary harmonic index n, the solution is expressed as:

$$A_z^{(\mathrm{I})}(r,\theta) = \sum_{n=1,3,5\ldots}^{nh} \begin{bmatrix} C_{a1,n} r^{np} + C_{a2,n} r^{-np} \\ +\Gamma_{1\_part}(r,n) \end{bmatrix} \sin(np\theta)$$

$$+ \sum_{n=1,3,5\ldots}^{nh} \begin{bmatrix} C_{a3,n} r^{np} + C_{a4,n} r^{-np} \\ +\Gamma_{2\_part}(r,n) \end{bmatrix} \cos(np\theta) \tag{3a}$$

For odd harmonic orders, the particular solutions, including the resonant case $np = 1$, are:

$$\Gamma_{1\_part}(r,n) = \begin{cases} \frac{np \cdot M_{nr}^c \cdot r - M_{n\theta}^s \cdot r}{(np)^2 - 1}, & np \neq 1 \\ \frac{M_{nr}^c \cdot r - M_{n\theta}^s}{2} r \ln(r), & np = 1 \end{cases} \tag{3b}$$

$$\Gamma_{2\_part}(r,n) = \begin{cases} \frac{-np \cdot M_{nr}^s \cdot r - M_{n\theta}^c \cdot r}{(np)^2 - 1}, & np \neq 1 \\ \frac{-M_{nr}^s \cdot r - M_{n\theta}^c}{2} r \ln(r), & np = 1 \end{cases} \tag{3c}$$

In the SD, the unknown coefficients $C_{a1,n}$, $C_{a2,n}$, $C_{a3,n}$, and $C_{a4,n}$ in (3a) are determined by enforcing boundary conditions [20, 21].

In the air-gap region (SD II), the absence of current sources reduces the system to Laplace's equation, and the homogeneous solution of (1c) is:

$$A_z^{(\mathrm{II})}(r,\theta) = \sum_{n=1,3,5\ldots}^{nh} \left[C_{e1,n} r^{np} + C_{e2,n} r^{-np}\right] \sin(np\theta)$$

$$+ \sum_{n=1,3,5\ldots}^{nh} \left[C_{e3,n} r^{np} + C_{e4,n} r^{-np}\right] \cos(np\theta) \tag{4a}$$

In the stator slot region (SD III), this SD is partitioned into Q_S elementary slots. For a given slot index i, the angular opening is centered around $\theta = g_i$, and the solution of (1d) is written as:

$$\begin{aligned} A_z^{(\mathrm{III})}(r,\theta) = {} & C_{i1} + C_{i2} \ln(r) - \frac{1}{4}\mu_0 j_z r^2 \\ & + \sum\nolimits_m C_{im} \cos\left[\beta_m \left(\theta - g_i + \frac{w_s}{2}\right)\right] \\ & + \sum\nolimits_v C_{iv} \sin\left[\gamma_v \ln\left(\frac{R}{R_2}\right)\right] \end{aligned} \tag{4b}$$

where:

$$C_{im} = C_{i3m}\left(\frac{R}{R_3}\right)^{\beta_m} + C_{i4m}\left(\frac{R}{R_2}\right)^{-\beta_m} \tag{4c}$$

$$\begin{aligned} C_{iv} = {} & C_{i5v}\frac{\sinh\left[\gamma_v\left(\theta - g_i + \frac{w_s}{2}\right)\right]}{\sinh(\gamma_v \cdot w_s)} \\ & + C_{i6v}\frac{\sinh\left[\gamma_v\left(\theta - g_i - \frac{w_s}{2}\right)\right]}{\sinh(\gamma_v \cdot w_s)} \end{aligned} \tag{4d}$$

where j_z is the current density in the stator slots; w_s is the slot opening arc; g_i is the slot position; β_m and γ_v are slot harmonic frequencies specified as follows:

$$\beta_m = \frac{m\pi}{w_s} \tag{4e}$$

and

$$\gamma_v = \frac{v\pi}{\ln\left(\frac{R_3}{R_2}\right)} \tag{4f}$$

where m and v represent spatial harmonic orders in the θ and r axes, respectively.

3. BOUNDARY CONDITIONS (BC)

Solving the analytical system requires defining BCs that ensure continuity of the magnetic vector potential, along with radial and tangential components of the magnetic field across adjacent regions [21, 29, 37].

3.1. Interface $r = R_0$

At the inner radius of the PMs, the rotor core is treated as infinitely permeable, and this assumption implies a purely radial magnetic field [20, 29], leading to a homogeneous Neumann condition:

$$\left.\frac{\partial A_z^{(\mathrm{I})}}{\partial r}\right|_{R_0} = 0 \tag{5a}$$

which gives:

$$npC_{a1,n}R_0^{np-1} - npC_{a2,n}R_0^{-np-1} + \left.\frac{d\Gamma_{1\_part}}{dr}\right|_{R_0} = 0 \tag{5b}$$

$$npC_{a3,n}R_0^{np-1} - npC_{a4,n}R_0^{-np-1} + \left.\frac{d\Gamma_{2\_part}}{dr}\right|_{R_0} = 0 \tag{5c}$$

3.2. Interface $r = R_1$

- Continuity of vector potential:

$$A_z^{(\mathrm{I})}(R_1, \theta) = A_z^{(\mathrm{II})}(R_1, \theta) \tag{6a}$$

which gives:

$$C_{a1,n}R_1^{np} + C_{a2,n}R_1^{-np} + \Gamma_{1\_part}(R_1, n) = C_{e1,n}R_1^{np} + C_{e2,n}R_1^{-np} \tag{6b}$$

$$C_{a3,n}R_1^{np} + C_{a4,n}R_1^{-np} + \Gamma_{2\_part}(R_1, n) = C_{e3,n}R_1^{np} + C_{e4,n}R_1^{-np} \tag{6c}$$

- Continuity of the tangential field:

$$H_\theta^{(\mathrm{I})}(R_1, \theta) = H_\theta^{(\mathrm{II})}(R_1, \theta) \tag{6d}$$

By applying (6d), the following relation is obtained

$$\frac{1}{\mu_0}\left(np\left(C_{a1,n}R_1^{np-1} - C_{a2,n}R_1^{-np-1}\right) + \left.\frac{d\Gamma_{1\_part}}{dr}\right|_{R_1}\right) = \left(npC_{e1,n}R_1^{np-1} - npC_{e2,n}R_1^{-np-1}\right) \tag{6e}$$

$$\frac{1}{\mu_0}\left(np\left(C_{a3,n}R_1^{np-1} - C_{a4,n}R_1^{-np-1}\right) + \left.\frac{d\Gamma_{2\_part}}{dr}\right|_{R_1}\right) = \left(npC_{e3,n}R_1^{np-1} - npC_{e4,n}R_1^{-np-1}\right) \tag{6f}$$

3.3. Interface $r = R_2$

- Continuity of vector potential:

$$A_z^{(\mathrm{II})}(R_2, \theta) = A_z^{(\mathrm{III})}(R_2, \theta) \tag{7a}$$

The condition of (7a) provides the following equations for coefficients:

$$C_{i1} + C_{i2}\ln(R_2) - \frac{1}{4}\mu_0 j_z R_2^2 = \frac{1}{w_s}\int_{g_i - \frac{w_s}{2}}^{g_i + \frac{w_s}{2}} A_z^{(\mathrm{II})}(R_2, \theta)\, d\theta \tag{7b}$$

$$C_{i3m}\left(\frac{R_2}{R_3}\right)^{\beta_m} + C_{i4m} = \frac{2}{w_s}\int_{g_i - \frac{w_s}{2}}^{g_i + \frac{w_s}{2}} A_z^{(\mathrm{II})}(R_2, \theta) \cos\left[\beta_m\left(\theta - g_i + \frac{w_s}{2}\right)\right] d\theta \tag{7c}$$

- Continuity of the tangential field:

$$H_\theta^{(\mathrm{II})}(R_2, \theta) = H_\theta^{(\mathrm{III})}(R_2, \theta) \tag{7d}$$

The condition in (7d) provides the following equations:

$$-\frac{1}{\mu_0}np \cdot \left(C_{e1,n}R_2^{np-1} - C_{e2,n}R_2^{-np-1}\right) = \frac{1}{\pi}\sum_{i=1}^{Q_s}\int_{g_i - \frac{w_s}{2}}^{g_i + \frac{w_s}{2}} H_\theta^{(\mathrm{III})}(R_2, \theta)\sin(np\theta)\, d\theta \tag{7e}$$

$$-\frac{1}{\mu_0}np \cdot \left(C_{e3,n}R_2^{np-1} - C_{e4,n}R_2^{-np-1}\right) = \frac{1}{\pi}\sum_{i=1}^{Q_s}\int_{g_i - \frac{w_s}{2}}^{g_i + \frac{w_s}{2}} H_\theta^{(\mathrm{III})}(R_2, \theta)\cos(np\theta)\, d\theta \tag{7f}$$

4. HYBRID MODELING USING 2D MEC

This section introduces a hybrid analytical model (HAM) that couples the SD framework with a MEC to accurately account for saturation-induced magnetomotive force (MMF) drops. The coupling is established using boundary flux-source injection as shown in Figure 2. The MEC discretizes the magnetic domain, representing each stator tooth and yoke

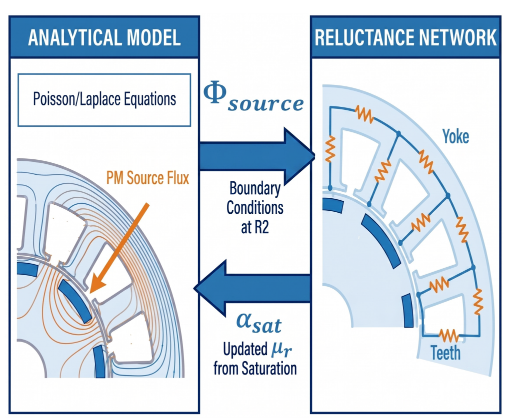

FIGURE 2. The basis of the hybrid SD-MEC model.

segment as a nonlinear variable reluctance, which depends on the local relative permeability [38] defined as:

$$\mathcal{R} = \frac{L}{\mu_0 \mu_r S} \tag{8a}$$

where L is the length of the magnetic path; S is the cross-sectional area traversed; and μ_r is the local relative permeability.

5. NODAL FORMULATION AND GLOBAL MATRIX

Once elemental reluctances are evaluated following detailed analytical formulations in Appendix A, they are interconnected to form a complete magnetic network, leading to a system of nodal equations solved iteratively. Within this structure, a scalar magnetic potential is assigned to the nodes at each reluctance terminal, whereas the PMs are modeled as equivalent flux sources injected at designated interface nodes. By applying the principle of flux conservation, which is conceptually similar to Kirchhoff's laws at each node, the global governing equation is formulated as follows:

$$\sum_j \frac{F_i - F_j}{\mathcal{R}_{i,j}} = \phi_{source,i}(t) \tag{8b}$$

where F_i and F_j are the scalar magnetic potentials at node i and its adjacent j, respectively, and $\mathcal{R}_{i,j}$ denotes the reluctance of the connecting branch. This mathematical framework results in a global system of nonlinear equations, represented as:

$$[P][F] = [\phi] \tag{8c}$$

where $[P]$ represents the permeance matrix, which aggregates coefficients for all nodes; $[F]$ denotes the vector containing scalar magnetic potentials for every node in the network; and $[\phi]$ is the source vector representing the magnetic flux injected at interface nodes, which is obtained directly from analytical calculations of the air gap.

6. RESOLUTION ALGORITHM AND SATURATION MANAGEMENT

A nested iterative procedure was employed to solve the hybrid model. Within this framework, the relative magnetic permeability is updated as a nonlinear function of local magnetic flux density. The final solution for the coupled system in (8c) was achieved using the iterative workflow shown in Figure 3. In this algorithm, the saturation factor α_{sat} quantifies the utilization of the magnetic circuit, directly reflecting potential degradation due to nonlinearities. This coefficient is defined as the ratio of the theoretical magnetic energy evaluated under the assumption of a perfectly linear, unsaturated core to the actual total magnetic energy stored in the system, expressed as:

$$\alpha_{sat} = \frac{W_{air}}{W_{air} + W_{teeth} + W_{yoke} + W_{leak}} \tag{9}$$

where W_{air}, W_{teeth}, W_{yoke}, and W_{leak} are magnetic energies stored in the air gap, stator teeth, stator yoke, and leakage regions, respectively, as detailed in Appendix B.

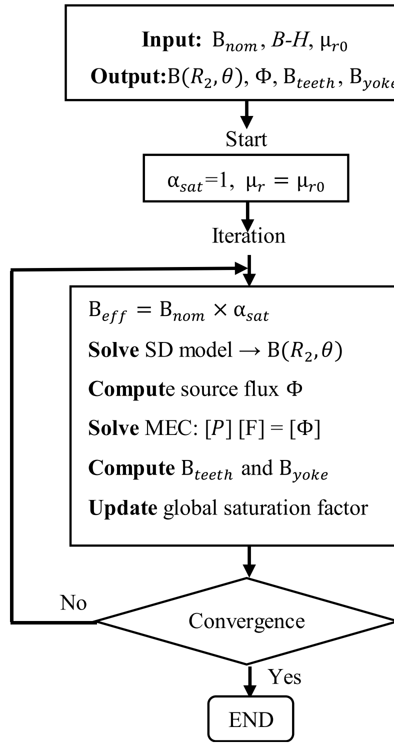

FIGURE 3. Flowchart of the iterative resolution algorithm.

7. FLUX LINKAGE AND BACK ELECTROMOTIVE FORCE

Using Stokes theorem, the flux linkage can be evaluated from the A_z distribution in region III according to:

$$\phi_i(t) = \frac{N_s L_s}{S} \int_{g_i - \frac{w_s}{2}}^{g_i + \frac{w_s}{2}} \int_{R_2}^{R_3} A_z^{(\mathrm{III})}(r, \theta, t)\, r dr d\theta \tag{10a}$$

where L_s is the axial length of the machine; S is the area of the stator slot; and N_s is the number of conductors. The phase flux vector is given by:

$$\begin{bmatrix} \phi_a \\ \phi_b \\ \phi_c \end{bmatrix} = C \begin{bmatrix} \phi_1 & \phi_2 & \cdots & \cdots & \phi_{Q_s} \end{bmatrix}^T \tag{10b}$$

where C is the $3 \times Q_s$ topological winding connection matrix mapping the individual slot fluxes to the phase flux linkages, whose elements are $+1$, -1, or 0 depending on the winding direction of a specific phase in a given slot, and the superscript T denotes the transpose.

Based on the Faraday-Lenz law, the three-phase back-EMF can be derived as:

$$\begin{bmatrix} E_a \\ E_b \\ E_c \end{bmatrix} = -\Omega \frac{d}{d\theta} \begin{bmatrix} \phi_a \\ \phi_b \\ \phi_c \end{bmatrix} \tag{10c}$$

where Ω is the rotor's electrical angular speed in rad/s, which is analytically related to the rated mechanical rotational speed

TABLE 2. Parameters of studied machines.

Symbol	Parameter	Value (unit)	Symbol	Parameter	Value (unit)
R_0	Rotor inner radius	1000 mm	Q_s	Number of stator slots	156
R_1	Magnet outer radius	1015 mm	p	Number of pole pairs	26
R_2	Stator bore radius	1020 mm	L_s	Active length	1000 mm
R_3	Slot bottom radius	1100 mm	w_s	Slot opening angle	$3\pi/4Q_s$
R_4	Stator outer radius	1160 mm	B_r	Magnet remanence	1.3 T
E_a	Magnet thickness	15 mm	β	Magnet fill factor	4/5
E_f	Air-gap thickness	5 mm	N_{nom}	Nominal speed	20 rpm
H_y	Yoke height	60 mm	nh	Number of harmonics	120

TABLE 3. Comparative performance and computational time validation.

Metric	Linear HAM	Proposed Nonlinear HAM	Linear FEA (FEMM 4.2)	Nonlinear FEA (FEMM 4.2)
Static field computation (B_r and B_θ)	3 seconds	9.5 seconds	3 minutes	11 minutes
Dynamic back-EMF computation (Full period)	7 minutes	18 minutes	4 hours	22 hours
Back-EMF THD (%)	12.64%	34.10%	∼12.64% (Reference match)	∼34.10 % (Reference match)
Magnetic flux linkage	Sinusoidal	Flattened peak	Sinusoidal	Flattened peak

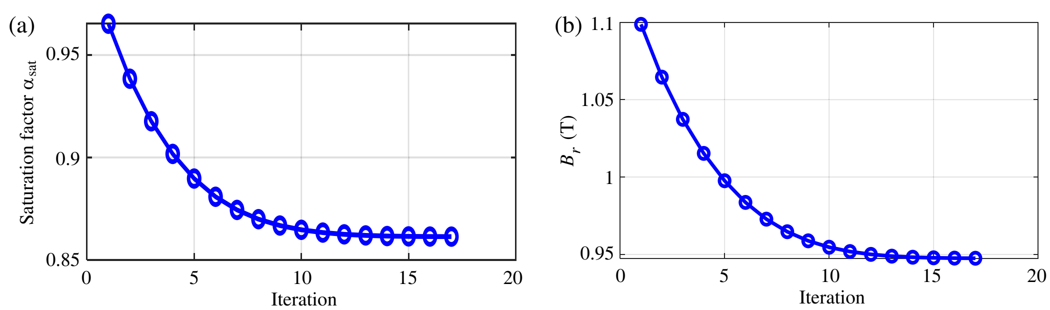

FIGURE 4. Iterative convergence process: (a) saturation factor α_{sat} and (b) radial magnetic flux density B_r in the middle of the air gap.

N_{nom} and the number of pole pairs p by the following expression

$$\Omega = p\,\frac{2\pi N_{nom}}{60} \tag{10d}$$

The total harmonic distortion (THD) can be calculated by:

$$\text{THD} = \frac{\sqrt{\sum_n^{20} h\,(n)^2}}{h(1)} \times 100 \tag{10e}$$

where $h(n)$ is the amplitude of the nth harmonic, and $h(1)$ is the fundamental harmonic.

8. NUMERICAL RESULTS AND VALIDATION

Designed for high-power wind turbine applications operating at a nominal speed of 20 rpm, the studied machine allowed an assessment of its nonlinear magnetic behavior. The previously established iterative algorithm was applied to evaluate the magnetic flux density waveforms for the specific configuration, detailed in Table 2. To compute the air-gap fields, an exact analytical SD formulation was employed, retaining 120 spatial harmonics, while the ferromagnetic regions were characterized by a 2D MEC that integrated the saturation profile derived from the M400-50A electrical steel B-H curve. The spatial discretization is structured with 5×5 elements per stator tooth and 10×10 elements per yoke segment, establishing an optimal balance between numerical precision and computational overhead. The proposed HAM yields results that demonstrate excellent agreement with the FEA reference using FEMM 4.2. To quantitatively justify the proposed method's superiority and efficiency, Table 3 summarizes analytical comparative results. The data demonstrate that the proposed nonlinear HAM strictly tracks the numerical FEA reference, accurately capturing the severe waveform degradation. More importantly, the table highlights the significant computational advantage of the hybrid approach. While static magnetic field evaluations re-

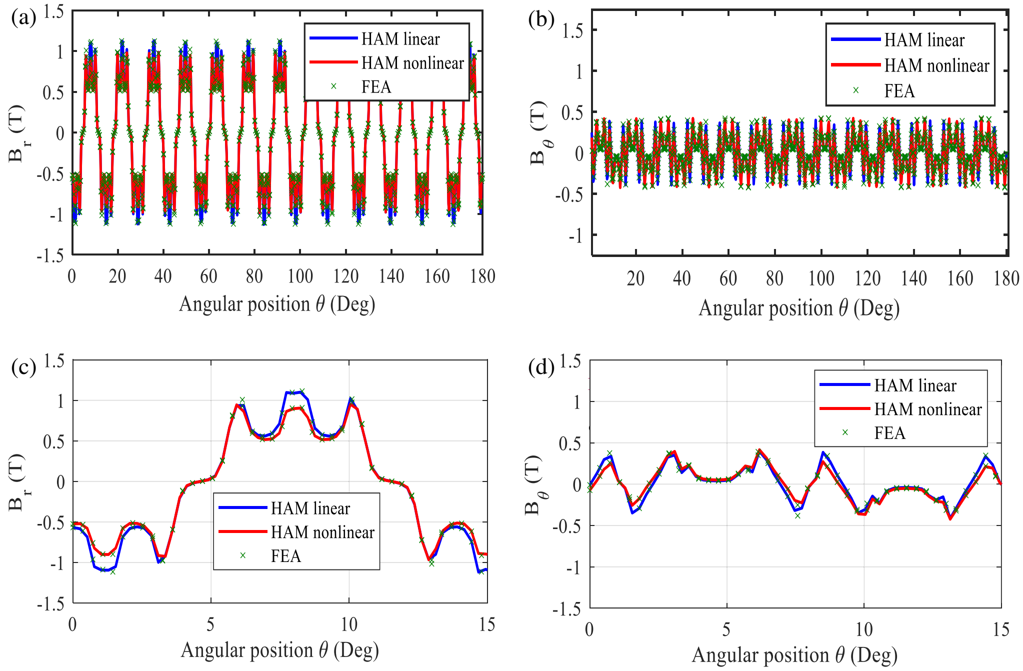

FIGURE 5. Air-gap magnetic flux density distribution in the middle of the air gap: (a) radial component B_r, (b) tangential component B_θ, and (c), (d) their respective zoomed-in views.

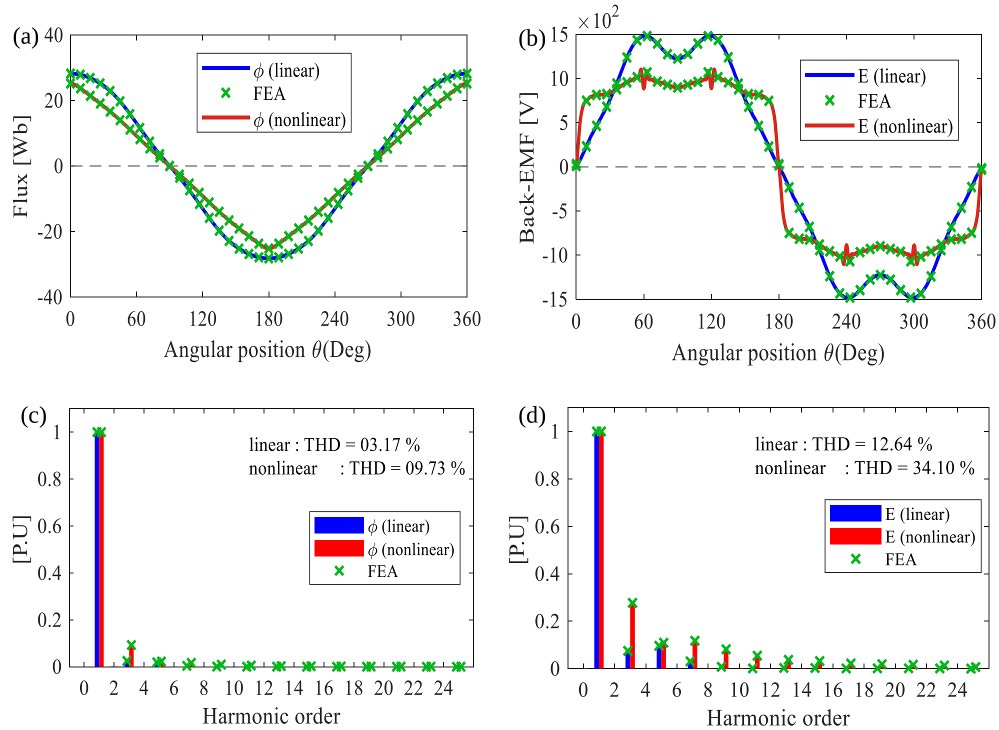

FIGURE 6. Single-phase electromagnetic performance and harmonic analysis calculated using the HAM and validated by FEA: (a) flux linkage ϕ profile, (b) back-EMF E profile, and (c), (d) their respective harmonic spectra.

quire only 9.5 s in HAM compared to 11 minutes for nonlinear FEA, the time-stepping dynamic evaluation of the back-EMF over a complete electrical period is dramatically reduced from an intensive 22 hours in nonlinear FEA to just 18 minutes using the proposed HAM. This rigorous validation confirms that the proposed method delivers FEA-level accuracy while drastically reducing the computational burden, making it highly suitable for iterative optimization processes.

The iterative algorithm converged rapidly within 17 iterations (Figures 4(a) and 4(b)). The initial sharp decrease in the saturation factor and radial flux density B_r reflects the material nonlinearity in the stator teeth and yoke. This rapid stabilization confirms the algorithm's numerical robustness in dynamically updating the localized permeabilities until a steady magnetic operating point is reached. Figure 5 shows air-gap magnetic flux density distributions, comprising both radial B_r and tangential B_θ components. As observed, accounting for magnetic saturation in the HAM leads to a visible flattening of the waveforms, which reduces the peak amplitudes compared to the linear predictions. Physically, as local permeability decreases due to saturation, increased reluctance restricts the main flux, causing clipping of B_r and localized redistribution of fringing flux in B_θ. The zoomed-in profiles (Figures 5(c) and 5(d)) show that the nonlinear HAM accurately tracks the FEA reference and reproduces high-frequency ripples, confirming the validity of the hybrid approach.

Figures 6(a)–(b) highlight the critical impact of magnetic saturation on the back-EMF. Although saturation inherently flattens the peak of the flux linkage (ϕ) (Figure 6(a)), its time-derivative nature radically distorts the back-EMF waveform (E), causing a significant drop in its peak amplitude (Figure 6(b)). This severe waveform degradation is quantified in harmonic spectra (Figures 6(c)–(d)): the flux THD increases from 3.17% (linear) to 9.73% (nonlinear), while the back-EMF THD surges from 12.64% under the linear assumption to 34.10% under nonlinear conditions, primarily driven by a pronounced 3rd harmonic. The exact superposition of the proposed nonlinear analytical model with the FEA results validates its accuracy in predicting saturation-induced distortions.

9. CONCLUSION

This study has proposed a fast 2D hybrid analytical approach to investigate the impact of magnetic saturation on the back-EMF in PMSMs. By coupling exact SD resolutions for linear domains with a nonlinear MEC for ferromagnetic regions, the method accurately models local saturation using M400-50A material characteristics. A key finding is that while local saturation flattens the magnetic flux density, the time-derivative relationship amplifies the induced harmonics, leading to significant distortion in the back-EMF waveform. The HAM's results demonstrated a strong agreement with those obtained from the FEA using FEMM 4.2, confirming the physical validity and accuracy of the SD-MEC model. Ultimately, this approach provides a reliable, computationally efficient tool, making it highly suitable for the parametric design and optimization of high-power PMSMs where saturation effects are critical.

ACKNOWLEDGEMENT

This work was supported by the General Directorate of Scientific Research and Technological Development (DGRSDT) of Algeria.

APPENDIX A.

The MEC is discretized into radial and tangential subdivisions for teeth ($N_{rad\_teeth} = 5$, $N_{tan\_teeth} = 5$) and yoke ($N_{rad\_yoke} = 10$, $N_{tan\_yoke} = 10$), which are interconnected

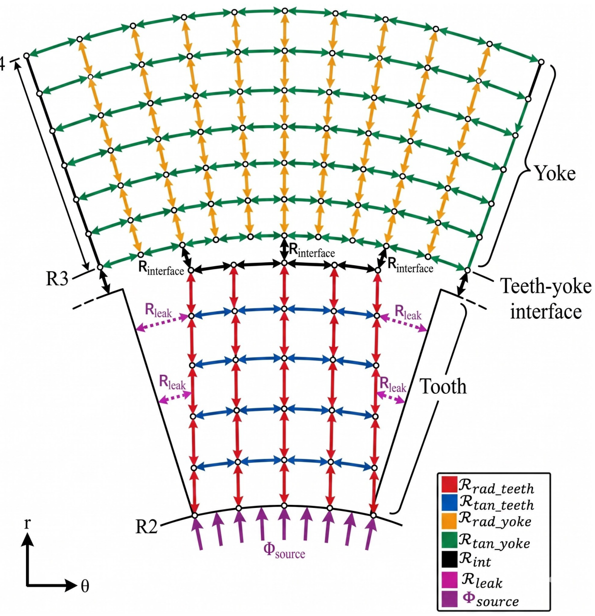

FIGURE A1. Modeling of the stator iron circuit by a reluctance network.

at radius R_3 by interface reluctances, alongside leakage reluctances between adjacent teeth (see Figure A1).

A.1. Radial Tooth Reluctance (r to $r+1$ Subdivision)

The radial reluctance of a tooth element is calculated by assuming a uniform permeability in the element, which can vary from one element to another, as follows:

$$\mathcal{R}_{rad}\left(i,r,t\right) = \frac{r_{out} - r_{in}}{\mu_0 \mu_r \left(i,r,t\right) \cdot \left(w_{sub} \cdot r_{mid}\right) \cdot L_s} \qquad \text{(A1)}$$

$\mathcal{R}_{rad}(i,r,t)$ represents the radial reluctance of the element located in tooth i, at radial division r and tangential column t where the element's mean radius is expressed as:

$$r_{mid} = \frac{r_{out} + r_{in}}{2} \qquad \text{(A2)}$$

and the tangential subdivision width is given by:

$$w_{sub} = \frac{w_{teeth}}{N_{tan\_teeth}} \qquad \text{(A3)}$$

A.2. Tangential Tooth Reluctance (t to $t+1$ at Level r)

The tangential reluctance, which represents the transverse leakage flux between two columns t and $t+1$ of the same tooth, is given by:

$$\mathcal{R}_{tan}\left(i,r,t\right) = \frac{w_{sub} \cdot r_{mid}}{\mu_0 \mu_r \left(i,r,t+1\right) \cdot h_{rad\_teeth}\left(r\right) \cdot L_s} \qquad \text{(A4)}$$

where the uniform radial height $h_{rad\_teeth}(r)$ is:

$$h_{rad\_teeth}\left(r\right) = \frac{R_3 - R_2}{N_{rad\_teeth}} \qquad \text{(A5)}$$

A.3. Tooth Yoke Interface at R_3

The connection between tooth tips ($r = R_3$) and the yoke was ensured by a geometric projection. Each tooth tip node is connected to the closest yoke node in the angular direction, ensuring flux conservation when the mesh density changes, where:

$$\mathcal{R}_{int} = \frac{(R_3 - R_2)/N_{rad\_teeth}}{\mu_0 \cdot \mu_r \cdot R_3 \cdot w_{sub} \cdot L_s} \tag{A6}$$

A.4. Slot Leakage Modeling

Unlike simplified models, flux leakages crossing the slot between two adjacent teeth are modeled by specific reluctances $\mathcal{R}_{leak}$. The reluctance is calculated based on the radial position within the slot.

The leakage path length in air at the radial position is the circular arc crossing the slot opening, and the effective arc length L_{leak} is expressed as:

$$L_{leak}(r) = w_s \cdot r \tag{A7}$$

The elementary passage cross-section corresponding to a radial division of height h_{rad_teeth} is:

$$S_{leak} = h_{rad\_teeth} \cdot L_s \tag{A8}$$

The leakage reluctance connecting the border node of tooth i to the border node of tooth $i+1$ is given by:

$$\mathcal{R}_{leak}(i, r) = \frac{L_{leak}(r)}{\mu_0 \cdot S_{leak}} \tag{A9}$$

APPENDIX B.

The ideal energy W_{air} corresponds to the energy stored in the magnetic circuit if all ferromagnetic parts are perfectly linear and unsaturated, and can be expressed as:

$$W_{air} = \frac{1}{2}\sum\nolimits_{i,t} \mathcal{R}_{air\_teeth} \left(\phi_{source\_R_2}(i,t)\right)^2 \tag{B1}$$

with:

$$\mathcal{R}_{air\_teeth} = \frac{E_f}{\mu_0 \cdot w_{teeth} \cdot r_{mid} \cdot L_s} \tag{B2}$$

where $\mathcal{R}_{air\_teeth}$ denotes the equivalent air region reluctance associated with a stator tooth, obtained by replacing the ferromagnetic tooth with an ideal air region having the same magnetic path length and cross-sectional area, and E_f is the effective flux tube length in the tooth region.

The magnetic energy stored in teeth W_{teeth} is calculated by summing elementary energy contributions of each reluctance in the network, which naturally captures the non-uniform, local saturation distribution in the stator core. Accordingly, the magnetic energy stored in the stator teeth is expressed as:

$$\begin{aligned} W_{teeth} = \sum_{i=1}^{Q_s}\sum_{r,t}\Bigg[&\frac{1}{2}\frac{(\Delta F_{rad\_teeth})^2}{\mathcal{R}_{rad\_teeth}(i,r,t)} \\ &+\frac{1}{2}\frac{(\Delta F_{tan\_teeth})^2}{\mathcal{R}_{tan\_teeth}(i,r,t)}\Bigg] \end{aligned} \tag{B3}$$

where ΔF is the local magnetomotive force drop across the considered reluctance element (radial or tangential branch).

Similarly, the energy stored in the yoke W_{yoke} is obtained by summing all sectors, including the flux closure reluctances:

$$\begin{aligned} W_{yoke} = \sum_{j=1}^{Q_s}\sum_{r,t}\Bigg[&\frac{1}{2}\frac{(\Delta F_{rad\_yoke})^2}{\mathcal{R}_{rad\_yoke}(j,r,t)} \\ &+\frac{1}{2}\frac{(\Delta F_{tan\_yoke})^2}{\mathcal{R}_{tan\_yoke}(j,r,t)}\Bigg] \end{aligned} \tag{B4}$$

The leakage energy W_{leak} accounts for flux paths outside primary magnetic circuits and is computed through dedicated leakage reluctances in peripheral network regions as follows:

$$W_{leak} = \sum_{i=1}^{Q_s}\sum_{r=1}^{N_{rad\_teeth}} \frac{1}{2}\frac{(F_{teeth}(i) - F_{teeth}(i+1))^2}{\mathcal{R}_{leak}(i,r)} \tag{B5}$$

REFERENCES

[1] Sun, S., S. Yu, Y. Zhang, Y. Song, and F. Zhang, "Review of low-speed high-torque permanent magnet direct-drive motors," *Chinese Journal of Electrical Engineering*, Vol. 12, No. 1, 216–239, 2026.

[2] Xiao, T., Z. Q. Zhu, Z. Azar, and N. Madani, "Comparative study of PMSG, EESG, and HESG for wind power application of different power levels," *IEEE Access*, Vol. 14, 64 920–64 934, 2026.

[3] Dong, Z., M. Jiang, S. Niu, and K. T. Chau, "Overview of permanent magnet wind power generators," *IEEE Transactions on Magnetics*, Vol. 61, No. 9, 1–11, 2025.

[4] Larabi, Z., K. Ghedamsi, and D. Aouzellag, "Direct drive permanent magnet synchronous generator: Design, modeling, and control for wind energy applications," *Periodica Polytechnica Electrical Engineering and Computer Science*, Vol. 68, No. 2, 168–177, 2024.

[5] Hoang, T.-K., L. Vido, and C. Tchuanlong, "Torque ripple and mass comparison between 20 MW rare-earth and ferrite permanent magnet wind generators," *Machines*, Vol. 11, No. 12, 1063, 2023.

[6] Jung, S.-W., D. Kang, K. Palanimuthu, Y. H. Joo, and S.-Y. Jung, "Design of 20 MW direct-drive permanent magnet synchronous generators for wind turbines based on constrained many-objective optimization," *Wind Energy*, Vol. 27, No. 9, 847–872, 2024.

[7] Wu, L. J., Z. Li, X. Huang, Y. Zhong, Y. Fang, and Z. Q. Zhu, "A hybrid field model for open-circuit field prediction in surface-mounted PM machines considering saturation," *IEEE Transactions on Magnetics*, Vol. 54, No. 6, 1–12, 2018.

[8] Wang, L., S. Zhang, W. Cai, B. Li, Z. Zhan, N. Bianchi, and A. Boglietti, "A novel multistructure equivalent magnetic network model for PMSM with enhanced magnetic field analysis and saturation compensation," *IEEE Transactions on Transportation Electrification*, Vol. 11, No. 5, 11 692–11 700, 2025.

[9] Azar, Z., Z. Q. Zhu, and G. Ombach, "Influence of electric loading and magnetic saturation on cogging torque, back-EMF and torque ripple of PM machines," *IEEE Transactions on Magnetics*, Vol. 48, No. 10, 2650–2658, 2012.

[10] Yousefnejad, S., M. Mehrasa, and P. Rastgoufard, "Magnetic equivalent circuit modeling and design of permanent magnet synchronous machines with distributed windings in axial-radial rotor configuration," *Energies*, Vol. 19, No. 4, 881, 2026.

[11] Li, Z., L. Wu, Y. Li, Q. Lu, X. Huang, L. Peretti, and Y. Shen, "Hybrid analytical model of permanent magnet linear motor considering iron saturation and end effect," *IEEE Transactions on Energy Conversion*, Vol. 39, No. 3, 2008–2017, 2024.

[12] Liu, L., Z. Li, H. Kang, Y. Xiao, L. Sun, H. Zhao, Z. Q. Zhu, and Y. Ma, "Review of surrogate model assisted multi-objective design optimization of electrical machines: New opportunities and challenges," *Renewable and Sustainable Energy Reviews*, Vol. 215, 115609, 2025.

[13] Dianati, B. and I. Hahn, "Nonlinear modeling of MGSPMs based on hybrid subdomain and magnetic equivalent circuitry," *IEEE Transactions on Magnetics*, Vol. 58, No. 1, 1–10, 2022.

[14] Du, W., L. Sun, and Z. Ma, "Multiphysics coupling analysis and structure optimization of flux switching permanent magnet linear motors," *Scientific Reports*, Vol. 15, No. 1, 21001, 2025.

[15] Jamali-Fard, A., M. Mirsalim, T. Sharifi, and N. Majlesi, "EMDLAB: An open-source finite element package for electromagnetic analysis of electrical machines," *SoftwareX*, Vol. 32, 102446, 2025.

[16] Jamali-Fard, A. and M. Mirsalim, "A robust numerical method for drawing the fluid flux-barrier geometry in the inner and outer rotor radial flux synchronous reluctance machines based on the finite difference method," *COMPEL*, Vol. 42, No. 2, 565–584, 2023.

[17] Lei, G., J. Zhu, Y. Guo, C. Liu, and B. Ma, "A review of design optimization methods for electrical machines," *Energies*, Vol. 10, No. 12, 1962, 2017.

[18] Zhu, Y., T. Peng, C. Zhu, and C. Mei, "A fast hybrid analytical model of PM machine with Halbach magnets and saturation effects," *Journal of Magnetics*, Vol. 31, No. 1, 79–90, 2026.

[19] Fang, C., L. Guo, J. Jiang, B. Wang, and W. Lu, "Multi-objective optimization of a modular unequal tooth-shoe PMLSM via an ARD-kriging surrogate-assisted framework," *Applied Sciences*, Vol. 16, No. 7, 3218, 2026.

[20] Zhu, Z. Q., L. J. Wu, and Z. P. Xia, "An accurate subdomain model for magnetic field computation in slotted surface-mounted permanent-magnet machines," *IEEE Transactions on Magnetics*, Vol. 46, No. 4, 1100–1115, 2010.

[21] Dubas, F. and C. Espanet, "Analytical solution of the magnetic field in permanent-magnet motors taking into account slotting effect: No-load vector potential and flux density calculation," *IEEE Transactions on Magnetics*, Vol. 45, No. 5, 2097–2109, 2009.

[22] Tiang, T. L., D. Ishak, C. P. Lim, and M. R. Mohamed, "Analytical method using virtual PM blocks to represent magnet segmentations in surface-mounted PM synchronous machines," *Progress In Electromagnetics Research B*, Vol. 76, 23–36, 2017.

[23] Li, Z., X. Huang, A. Liu, Z. Liu, L. Wu, and T. Shi, "Analytical model of electromagnetic performance for permanent-magnet vernier machines using nonlinear exact conformal model," *IEEE Transactions on Transportation Electrification*, Vol. 8, No. 2, 2005–2014, 2022.

[24] Bapiri, M., A. Vahedi, and H. A. Moghaddam, "Analytical model for ring winding axial flux permanent magnet motor using Schwarz-Christoffel conformal mapping," *IET Electric Power Applications*, Vol. 19, No. 1, e70006, 2025.

[25] Roubache, L., K. Boughrara, F. Dubas, and R. Ibtiouen, "Semi-analytical modeling of spoke-type permanent-magnet machines considering the iron core relative permeability: Subdomain technique and Taylor polynomial," *Progress In Electromagnetics Research B*, Vol. 77, 85–101, 2017.

[26] Huang, J., Q. Sun, and C. Wang, "Analytical modeling and analysis of high-torque-density three-segment halbach array PM machine by considering leakage flux," *Machines*, Vol. 14, No. 6, 683, 2026.

[27] Nyitrai, A. and M. Kuczmann, "Magnetic equivalent circuit and finite element modelling of anisotropic rotor axial flux permanent magnet synchronous motors with fractional slot distributed winding," *IET Electric Power Applications*, Vol. 17, No. 5, 709–720, 2023.

[28] Hanic, A., D. Zarko, D. Kuhinek, and Z. Hanic, "On-load analysis of saturated surface permanent magnet machines using conformal mapping and magnetic equivalent circuits," *IEEE Transactions on Energy Conversion*, Vol. 33, No. 3, 915–924, 2018.

[29] Ladghem-Chikouche, B., K. Boughrara, F. Dubas, L. Roubache, and R. Ibtiouen, "Magnetic field calculation for flat permanent-magnet linear machines using a hybrid analytical model," *ENP Engineering Science Journal*, Vol. 1, No. 2, 1–8, 2021.

[30] Sun, Q., Q. Ren, Q. Zhan, and Q. H. Liu, "3-D domain decomposition based hybrid finite-difference time-domain/finite-element time-domain method with nonconformal meshes," *IEEE Transactions on Microwave Theory and Techniques*, Vol. 65, No. 10, 3682–3688, 2017.

[31] Ladghem Chikouche, B., K. Boughrara, F. Dubas, and R. Ibtiouen, "Two-dimensional hybrid model for magnetic field calculation in electrical machines: Exact subdomain technique and magnetic equivalent circuit," *COMPEL*, Vol. 40, No. 3, 535–560, 2021.

[32] Wu, L., H. Yin, D. Wang, and Y. Fang, "A nonlinear subdomain and magnetic circuit hybrid model for open-circuit field prediction in surface-mounted PM machines," *IEEE Transactions on Energy Conversion*, Vol. 34, No. 3, 1485–1495, 2019.

[33] Wu, L., H. Yin, D. Wang, and Y. Fang, "On-load field prediction in SPM machines by a subdomain and magnetic circuit hybrid model," *IEEE Transactions on Industrial Electronics*, Vol. 67, No. 9, 7190–7201, 2020.

[34] Zhu, Y., G. Liu, L. Xu, W. Zhao, and D. Cao, "A hybrid analytical model for permanent magnet vernier machines considering saturation effect," *IEEE Transactions on Industrial Electronics*, Vol. 69, No. 2, 1211–1223, 2022.

[35] Cheng, M., X. Zhao, M. Dhimish, W. Qiu, and S. Niu, "A review of data-driven surrogate models for design optimization of electric motors," *IEEE Transactions on Transportation Electrification*, Vol. 10, No. 4, 8413–8431, 2024.

[36] Abbas, A., A. Iqbal, A. Lewicki, B. Prathap, and M. Mnzool, "A review on analytical models of brushless permanent magnet machines," *International Journal of Numerical Modelling: Electronic Networks, Devices and Fields*, Vol. 37, No. 2, e3133, 2024.

[37] Lubin, T., S. Mezani, and A. Rezzoug, "2-D exact analytical model for surface-mounted permanent-magnet motors with semi-closed slots," *IEEE Transactions on Magnetics*, Vol. 47, No. 2, 479–492, 2011.

[38] Silva, A. M., C. H. Antunes, A. M. S. Mendes, and F. J. T. E. Ferreira, "Generalized reluctance network framework for fast electromagnetic analysis of radial-flux machines," *IEEE Transactions on Energy Conversion*, Vol. 38, No. 1, 310–320, 2023.